sustainability

MDPI

Article

Spatiotemporal Distribution Characteristics of Fire Scars Further Prove the Correlation between Permafrost Swamp Wildfires and Methane Geological Emissions

Wei Shan [1,2,3,*], Lisha Qiu [1], Ying Guo [1,2,3], Chengcheng Zhang [1,2,3], Zhichao Xu [1] and Shuai Liu [1]

[1] Institute of Cold Regions Science and Engineering, Northeast Forestry University, Harbin 150040, China
[2] Ministry of Education Observation and Research Station of Permafrost Geo-Environment System in Northeast China (MEORS-PGSNEC), Harbin 150040, China
[3] Collaborative Innovation Centre for Permafrost Environment and Road Construction and Maintenance in Northeast China (CIC-PERCM), Harbin 150040, China
* Correspondence: shanwei@nefu.edu.cn

Abstract: Affected by global warming, methane gas released by permafrost degradation may increase the frequency of wildfires, and there are few studies on wildfires in permafrost regions and their correlation with climate and regional methane emissions. The northwestern section of the Xiaoxing'an Mountains in China was selected as the study area, and the spatial relationship between permafrost and spring wildfires was studied based on Landsat TM and Sentinel-2 data. Combined with monitoring data of air temperature, humidity, and methane concentration, the impact of methane emissions on spring wildfires was analyzed. The study shows that the spatial distribution of fire scars in spring is highly consistent with permafrost, and the change trend of fire scars is in line with the law of permafrost degradation. Wildfires occur intensively during the snow melting period in spring, and the temporal variation pattern is basically consistent with the methane concentration. The number of fire points was positively correlated with air temperature and methane concentration in March and April, and spring wildfires in permafrost regions are the result of a combination of rising seasonal temperatures, surface snow melting, and concentrated methane emissions. Larger areas of discontinuous permafrost are more prone to recurring wildfires.

Keywords: permafrost degradation; wildfire; methane emissions; climate change; correlation analysis

check for updates

Citation: Shan, W.; Qiu, L.; Guo, Y.; Zhang, C.; Xu, Z.; Liu, S. Spatiotemporal Distribution Characteristics of Fire Scars Further Prove the Correlation between Permafrost Swamp Wildfires and Methane Geological Emissions. *Sustainability* **2022**, *14*, 14947. https://doi.org/10.3390/su142214947

Academic Editor: Irene Petrosillo

Received: 31 July 2022
Accepted: 8 November 2022
Published: 11 November 2022

1. Introduction

Permafrost accounts for 24% of the land area of the Northern Hemisphere, is an important component of the forest and shrub ecosystems in the northern circumpolar region, and plays a critical role in the atmospheric carbon pool and source/sink budget [1–3]. The past three decades have seen a rapid increase in temperature at high latitudes (0.060 °C/a), twice the global average rate [4]. Climate warming has triggered widespread, sustained, and rapid permafrost thaw and wetland degradation [5]. On the Arctic, North Atlantic, and North Pacific continental shelves, methane is released from destabilizing hydrates, accompanied by climate warming and the warming of permafrost and oceans [6–8]. Permafrost regions may become a main source of major greenhouse gases (CO_2, CH_4, and N_2O). The emissions of major greenhouse gases such as CH_4 and CO_2 inevitably interfere with the structure and function of terrestrial systems and exacerbate global warming [9,10]. In addition, the greenhouse effect caused by methane gas emissions and its own highly explosive and spontaneous combustion characteristics may greatly increase the risk of regional fire events.

Fire is one of the main factors driving changes in boreal forest structure and species composition, and exerts extremely important effects on energy exchange, biogeochemistry, hydrology, and carbon and nitrogen cycles in forests [3,11]. Currently, the main factors affecting fire occurrence include sustained high temperature and dry weather, thunderstorms, strong winds, and artificial arson. A recent study has shown that climate warming and drying will lead to an increase in the frequency of wildfires [12]. Wildfires destroy the surface organic mats and vegetation that provide thermal protection, accelerating the formation of thermokarst terrain and the degradation of ice-rich permafrost. In addition, wildfires have an extensive and long-lasting impact on the thermal conditions of permafrost soils [13]. After a wildfire, the interactions among burn severity, terrain, and vegetation control the distribution of near-surface permafrost and related drainage conditions [14]. In turn, the degradation of permafrost and the deepening of the active layer promote the release of carbon stored in the permafrost, which will aggravate the carbon loss in high-latitude permafrost regions, leading to further disruption of the carbon balance in boreal and Arctic ecosystems and facilitating the transformation of carbon sinks into carbon sources [14–17].

The rapid development of remote sensing technology provides new ideas and methods for studying the mutual feedback relationship between permafrost and wildfires at fine scales and in real time [13,18]. Remote sensing data can provide detailed distribution information for the two at global, regional, and local geographic scales to assist in monitoring and analyzing their dynamics and interrelationships [19,20]. Permafrost in Northeast China is mainly found in the Daxing'an, Xiaoxing'an, and Changbai Mountain Range, and this high-latitude and mountainous permafrost is highly sensitive to climate change. The discontinuous permafrost in this region has degraded by 38% in recent decades due to climate warming, and the southern boundary of permafrost exhibits a clear northward-moving trend [21]. The frequency of climate-induced fires in this region is increasing year-by-year, which will not only further aggravate climate warming and permafrost degradation, but also affect the management, protection, and sustainable development of local forest resources. To date, studies on the relationship between permafrost degradation and wildfire have focused on the effects of wildfire events on permafrost thaw and carbon balance [14,15,22,23]. However, the mutual feedback relationship between wildfire and permafrost degradation remains poorly understood at regional scales. Therefore, more refined data and new research tools are needed to analyze the spatial and temporal correlations between the two.

This study selected the K153-K183 section of the Bei'an-Heihe Expressway in the northwestern Xiaoxing'an Mountains as the study area. The characteristics of spring wildfire spatiotemporal distribution during the 2017–2021 period are described based on field surveys, remote sensing information, and GIS analysis. Combined with permafrost distribution, topographic data, meteorology, and methane concentration monitoring data, the relationship between wildfires and climate and local methane emissions in permafrost regions is discussed. This study provides a reference for studying the causal mechanisms underlying fire occurrence and ecosystem carbon dynamics in boreal and Arctic permafrost regions in the context of temperature changes.

2. Materials and Methods

2.1. Study Region

The study area is located at the margin of the Sunwu-Jiayin Basin in the low-mountain and hilly landform area of the Xiaoxing'an Mountains. It is an intermountain permafrost swamp (Figure 1) with an altitude of 110–755 m and a total area of approximately 1585 km^2. The study area is characterized by a continental monsoon climate controlled by the Siberian-Mongolian high-pressure system in winter and influenced by the warm and humid Pacific airflow in summer, with an annual average air temperature of approximately −2 to 1 °C, an average annual precipitation of approximately 550 mm, and summer precipitation accounting for 65% of the total annual precipitation. The vegetation is dominated by cold-temperate coniferous forests and mixed coniferous/broad-leaved forests. The relatively low-lying area is a *Sphagnum* swamp with a widely distributed stable inversion layer, which has an important impact on the development and distributional characteristics of permafrost. This permafrost distribution with such special characteristics is referred to as Xing'an-Baikal permafrost [24–26]. Sentinel-2 satellite imagery has detected significant seasonal wildfires caused by greenhouse gas anomalies in this area in spring and autumn in recent years, and wildfires have occurred frequently in the study area, especially at the end of snow and ice melting in spring [27].

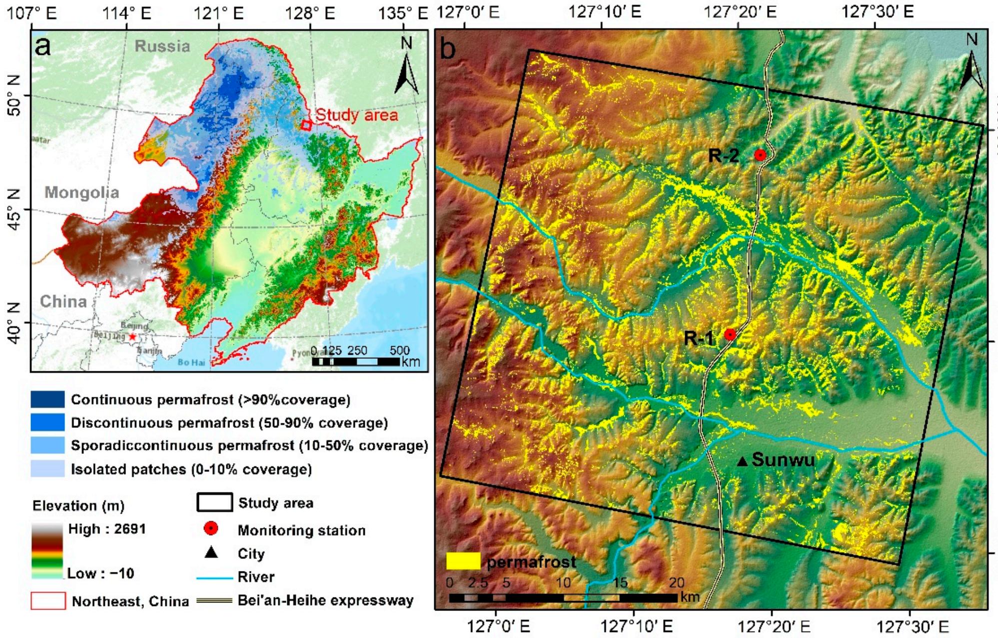

Figure 1. Geographical location and permafrost distribution of the study area. (**a**) Geographical location and permafrost distribution in Northeast China; the permafrost data are derived from S. Gruber's [28] global permafrost distribution results, there is no copyright issue, more details on "Copyright and Licensing" are available via the following link: https://www.geo.uzh.ch/microsite/cryodata/, accessed on 30 July 2022; (**b**) permafrost distribution and monitoring station locations in the study area.

This area is a swamp with high surface soil moisture after the spring thaw. Wildfire events were dominated by incomplete combustion of the surfaces of *Carex* tato plants. The *Carex* roots above the surface water burned to a greater degree, while those at the edge of the surface water burned to a lower degree or even remained unburned, showing a patchy and scattered burn overall (Figure 2g,h). In addition, there were regions with many microvolcano-like features in the study area (Figure 2i), where *Carex* tato burned heavily (visible as grey colour), which was due to variation in the extent of burning caused by methane gas from under the frozen layer breaking through the weak soil layer at high pressure, leading to high concentrations of methane discharged from the pores.

Permafrost in the study area covers approximately 215.81 km^2, accounting for 13.61% of the total study area. Seasonal permafrost and talik account for over 80%. The permafrost has a thickness of approximately 5–10 m, a mean annual ground temperature of 0.5–5.0 °C [27,29], and is mainly distributed in river valleys and on foothills and shady slopes; it is characterized by high temperature, small thickness, and extremely unstable hydrothermal state and is susceptible to disturbance by external environmental changes and human activities. The combined influence of regional geological conditions, climate change, and human activities results in drastic degradation of permafrost, which ranges in distribution with increasing elevation from local and discontinuous, to intermittent and island-like, and then sporadic [25,27].

Figure 2. Fire scars near the meteorological stations in the study area in April 2021, R-1 and R-2 meteorological stations, and the deployment environment. (**a**) The fire scar near the R-1 meteorological station in spring 2021. (**b**) The environmental conditions after the surface thaw at the R-1 meteorological station. (**c**) The R-1 meteorological station. (**d**) The fire scar near the R-1 meteorological station in spring 2021. (**e**) The scene of high-concentration methane release from a borehole in the swamp in the study area in spring. (**f**) The R-2 meteorological station. (**g**–**i**) Fire scars near the R-2 meteorological station in spring 2021.

2.2. Data Sources

Sentinel-2 data (https://apps.sentinel-hub.com/, accessed on 15 March 2021) were used to extract the fire scars in the study area from March to April of 2017–2021. This dataset contains 13 bands ranging from visible and near infrared to shortwave infrared, with image bands of different resolution that can satisfactorily meet the mapping requirements at different scales [30,31]. The pre-fire and post-fire cloud-free datasets for March of each year were selected separately, and the Sentinel-2 L1C data were radiometrically calibrated and atmospherically corrected using the Sentinel-2 Toolbox (Sentinel Application Platform, SNAP v2.4.0) to obtain L2A data. Table 1 shows the wildfire time period and Sentinel-2 image selection time.

Table 1. Sentinel-2 data selection times (YYYY-M-DD).

Data Source	Wildfire Occurrence Time	Image Selection Time
Sentinel-2	20 March 2017–27 March 2017	9 April 2017
Sentinel-2	25 March 2018–30 March 2018	30 March 2018
Sentinel-2	22 March 2019–1 April 2019	11 April 2019
Sentinel-2	19 March 2020–24 March 2020	5 April 2020
Sentinel-2	19 March 2021–21 March 2021	24 March 2021

The statistical data on the daily numbers of fires in the study area were derived from the Visible Infrared Imaging Radiometer Suite (VIIRS) thermal anomalies/active fire product. This data product (https://firms.modaps.eosdis.nasa.gov/, accessed on 15 March 2021) originated from the data captured by the VIIRS sensors onboard the joint National Aeronautics and Space Administration/National Oceanic and Atmospheric Administration (NOAA) Suomi National Polar-orbiting Partnership (Suomi NPP) and NOAA-20 satellites. The VIIRS Active Fire data have a spatial resolution of 375 m and a temporal resolution of $\leq$12 h. The data show good consistency with the Moderate Resolution Imaging Spectroradiometer (MODIS) data in hotspot detection, but the improved spatial resolution of VIIRS imagery provides greater response to fires in relatively small areas and enhanced nighttime performance, making it suitable for fire monitoring and management as well as other scientific applications requiring improved fire mapping fidelity.

A meteorological monitoring system (http://www.qixiangshuju.com, accessed on 20 March 2021) was used to monitor the site meteorological data in real time. The R-1 and R-2 meteorological stations (model GD24-YCXQ) are set up at altitudes of 278 m (127°18′21″ E, 49°30′52″ N) and 229 m (127°21′5″ E, 49°39′28″ N), respectively. Each station is mainly composed of a data acquisition host, a data analysis system, a data transmission system, Internet of Things sensors, a general packet radio service (GPRS) wireless transmission system, and a solar power supply system. The sensors mainly include surface meteorological element sensors such as surface methane concentration sensors (QT21-BX80-CH_4) and air temperature sensors (GD51-KWSY). Each meteorological station is equipped with three methane concentration sensors (CH_4-1, CH_4-2, and CH_4-3) that measure surface methane concentration in units of parts per million (ppm). The monitoring systems described above all use GPRS communication to transmit data to the central station periodically and generate messages automatically without human intervention, with high accuracy and reliability [27]. The monitoring stations and surrounding environment are shown in Figure 2.

The permafrost and surface temperature distribution data were obtained from a study by Wang et al. Landsat-7 ETM+ images from March (at the end of snow cover melt), May (when temperature was always above zero), and September (when the seasonal thaw depth was highest) of 2009 were selected. The surface temperature was obtained using the inverse function of the Planck formula. According to the criteria for determining permafrost islands, a map of permafrost distribution in the study area was further generated through methods such as threshold division and superposition analysis. The results obtained are highly accurate and consistent with the pattern of regional distribution of Xing'an-Baikal permafrost and with field permafrost drilling results [32].

2.3. Extraction of Fire Scars

Pre-fire and post-fire images are generally used to generate fire scar and fire severity indices such as the differenced normalized burn ratio (dNBR), relativized dNBR (RdNBR), relativized change in total fractional cover (RdFCT), change in bare fractional cover (dFCB), differenced normalized difference vegetation index (dNDVI), and differenced bare soil index (dBSI) [33]. Since wildfires in the study area occurred during the spring snow and ice melt, the dNBR and dNDVI-based methods for extracting fire scars are not effective in distinguishing fire scars from wet bare soils. Therefore, supervised classification was used to extract fire scars in this study. The shortwave infrared (SWIR) RGB composite band of the Sentinel-2 data was selected for use. SWIR is a composite of the B12, B8A, and B04 bands of the Sentinel-2 data and can accurately represent newly burned land. Therefore, it can be used to distinguish the fire scars within a short temporal range [34].

ENVI 5.3 software was used to divide the study area into six types of surface features (bare land, fire scars, vegetation, waterbodies, buildings, and farmland) by visual interpretation, and 100 training samples were selected for each type of surface feature (70% for classification and the remaining 30% for accuracy verification). The maximum likelihood method was used for supervised classification to extract fire scar information. Some waterbodies, vegetation, and bare land in the extraction results were misclassified as fire scars and removed using decision tree classification. Figure 3 shows the extraction process of spring wildfire burns in local areas in 2018, 2020, and 2021. The results were validated, with an overall accuracy of 82.71% and a kappa coefficient of 0.66, satisfying study requirements. The extraction results of fire scars based on Sentinel-2 data were used to analyze the spatial correlation between wildfires and permafrost.

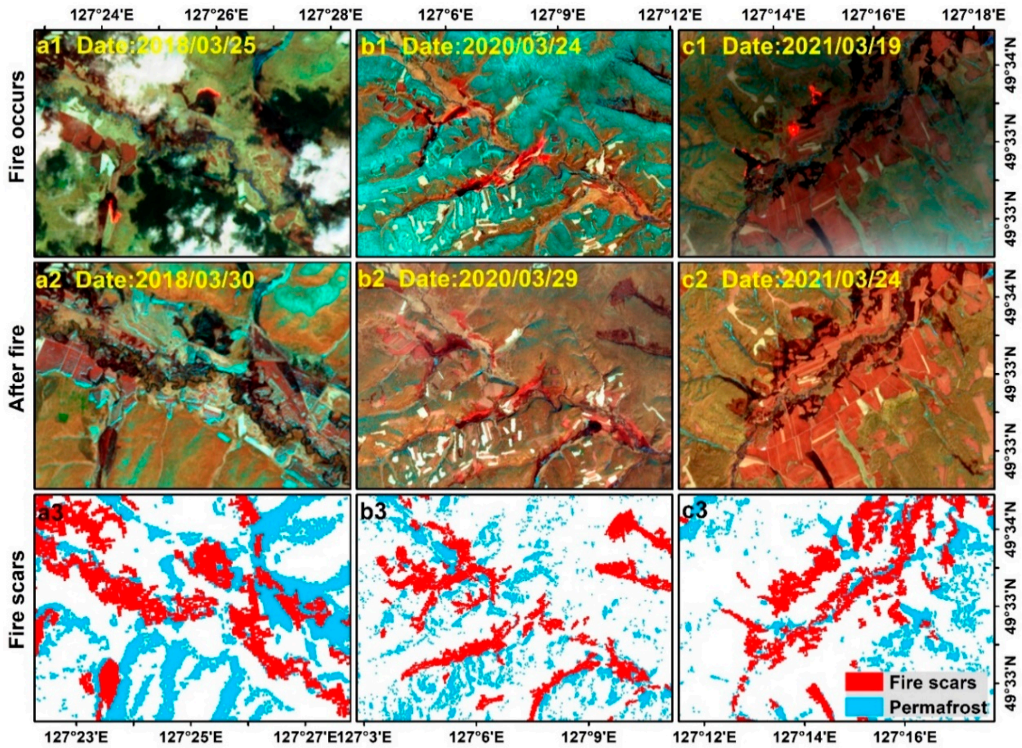

Figure 3. The local area fire events in March 2018, 2020, and 2021, the Sentinel-2 satellite remote sensing images of the burned areas, and the extraction results of the fire scars. (**a1**,**b1**,**c1**) Satellite remote sensing images of the fires on 25 March 2018, 24 March 2020, and 19 March 2021. (**a2**,**b2**,**c2**) The satellite remote sensing images of the burned areas after the fires on 30 March 2018, 29 March 2020, and 24 March 2021, respectively, with a spatial resolution of 20 m. (**a3**,**b3**,**c3**) The burnt areas extracted from the three images (**a2**,**b2**,**c2**), respectively. The red part is the burnt area, and the blue base map part is the permafrost.

2.4. Correlation Analysis

Correlation analysis was carried out to study the relationships of climatic factors and atmospheric methane concentration with wildfire occurrence frequency, with a focus on the correlations of air temperature, air humidity, and atmospheric methane concentration with the number of wildfires. The larger the absolute value of the correlation coefficient, the stronger the correlation of the number of wildfires with a climatic factor or methane concentration; conversely, the smaller the absolute value of the correlation coefficient, the lower the correlation between the two. The correlation coefficient is calculated as follows [35]:

$$r = \frac{\sum_{i=1}^{n}(a_i - \bar{a})\left(b_i - \bar{b}\right)}{\sqrt{\sum_{i=1}^{n}(a_i - \bar{a})^2\left(b_i - \bar{b}\right)^2}} \quad (1)$$

where n is the cumulative number of years in the monitoring period, a and b are the two variables included in the correlation analysis, and $\bar{a}$ and $\bar{b}$ are the mean values of the variables.

2.5. Overlay Analysis

Overlay analysis is a very important spatial analysis function in GIS, which refers to the process of generating new data through a series of collective operations on two data under the same spatial reference system. The goal of overlay analysis is to analyze the interrelationships between spatial features and exclusive attributes of spatial objects that are related in spatial locations [36]. In this study, we calculated the area of wildfires on permafrost and the location and area of repeated wildfires by superimposing and analyzing the vector data of wildfires and permafrost in ArcGIS software.

3. Results

3.1. Characteristics of Wildfire and Permafrost Spatial Distribution

The area of fire scars and the number of fires extracted based on the Sentinel-2 data were analyzed statistically, and the overlap between fire scars and permafrost was also extracted by the intersection method, as shown in Figure 4. The total area of fire scars in the study area in the spring from 2017 to 2021 ranged from 77.098 to 134.495 km^2, accounting for 4.9% to 8.5% of the total study area. The total area of fire scars was greatest in 2017, then decreased rapidly in the following two years and increased slightly in 2020. The total number of fires ranged between 124 and 251, which was consistent with the changes in the area of fire scars, with both declining over time. The overlap between the distribution of fire scars and that of permafrost accounted for 19.636% to 25.560% of the permafrost area in the study area.

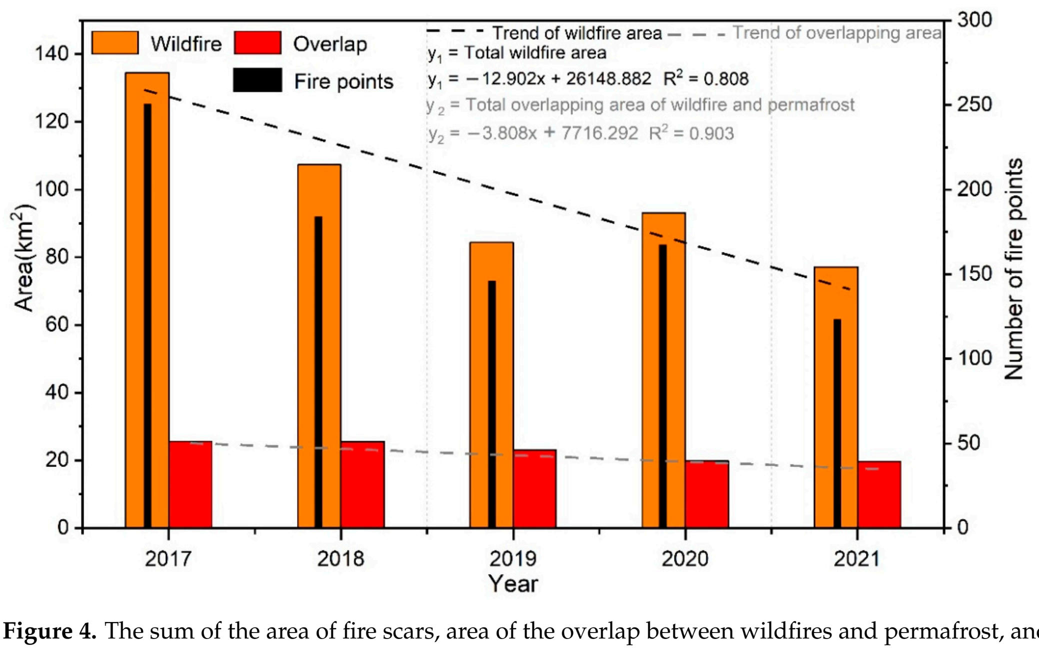

Figure 4. The sum of the area of fire scars, area of the overlap between wildfires and permafrost, and number of wildfires in the study area from March to April 2017 to 2021. The orange bars represent the areas of fire scars, the red bars represent the areas of the overlap between fire scars and permafrost, and the black bars represent the numbers of fires.

The spatial distribution of the fire scars is shown in Figure 5. In the spring, fires were widely distributed in the study area, and individual fires were small in size and patchily distributed. The spatial distribution of fire scars was highly consistent with that of permafrost, with most of them distributed on or around permafrost (island-like), and wildfires with large burning areas were mostly concentrated in low-lying areas such as valleys and river valley terraces at low altitudes in the central portion of the study area. The planar positions and altitudinal distribution of fires and permafrost indicate that the permafrost and wildfires were mostly distributed in the eastern and central parts of the study area, gradually increasing from west to east and from high to low altitudes. Because the terrain of the study area is high in the west and low in the east, the fire scars and permafrost in the west were mainly distributed in the altitude range of 250–400 m, while the altitudinal distribution of permafrost and fire scars in the eastern portion of the study area was significantly lower than that in the west and roughly between 200 and 300 m, with wildfires more densely distributed at lower altitudes.

3.2. Distributional Characteristics of Wildfires and Permafrost Topography

The permafrost in the study area was mostly distributed on north- and northwest-facing slopes, followed by northeast- and west-facing hillsides and valley bottoms (Figure 6a); low-lying swamps and shady gentle slopes at the bottoms of valleys are more conducive to protecting permafrost [37]. Wildfires and permafrost differed slightly in aspect distribution and mainly in 2017, when wildfires mainly occurred on the south-facing slopes (18.43%) and southeast-facing slopes (16.61%), followed by the north-facing slopes (15.02%) and northeast-facing slopes (13.31%). After 2017, the aspect distribution of wildfires tended to be consistent among years, with the greatest area on north-facing slopes, accounting for 16% to 19% of the total area of fire scars, followed by northeast-facing slopes, and the area of fire scars on south-facing slopes was slightly lower than that on north-facing slopes. It is generally believed that within the same valley, the south-facing slope receives the most solar radiation, followed by the southeast- and southwest-facing slopes, and the north-facing slope has the least solar radiation [25,37]. Therefore, the surface temperatures of the sunny slopes are higher than those of the shady slopes, which are slightly higher than those of the valley bottoms, leading to permafrost degradation first on the sunny slopes and then on the shady slopes and valleys, as was also the pattern of wildfire occurrence in this study area.

Terrain controls the Xing'an-Baikal permafrost more strongly than in Arctic and high-altitude permafrost. Terrain controls the redistribution of soil moisture in the horizontal and vertical directions and is an important factor controlling the distribution of permafrost as well as the vegetation and carbon storage of boreal forests and wetlands [38,39]. As shown in Figure 6b, permafrost was mainly found between 190 and 450 m, with peaks at 250, 280, 330, and 350 m. Moreover, above 250 m, the area of permafrost gradually decreased with increasing altitude. Wildfires and permafrost showed similar distribution patterns in terms of altitude and were mainly found between 180 and 420 m. The distribution of wildfires was similar among years but slightly different in the range of 240–270 m. The elevation with the highest fire scar area decreased from 265 m in 2018 to 240 m in 2021, gradually shifting to lower altitudes. This finding indicates a tendency for wildfires to spread from high to low altitudes over time, consistent with the pattern of the degradation of Xing'an-Baikal permafrost from mountains to valley bottoms [40]. The relatively high surface temperature on the upper part of a hillside due to effective drainage and greater sunlight exposure results in the degradation of permafrost at the top of the hillside before permafrost at the bottom degrades as well as drier soils, increasing the flammability of the fuel and making it more likely to burn. The distribution of wildfires and permafrost in terms of slope (Figure 6c) showed that the fire scars and permafrost in different years were mostly found at slopes of 0–6°; the areas of fire scars and permafrost gradually declined with increasing slope and the passage of time.

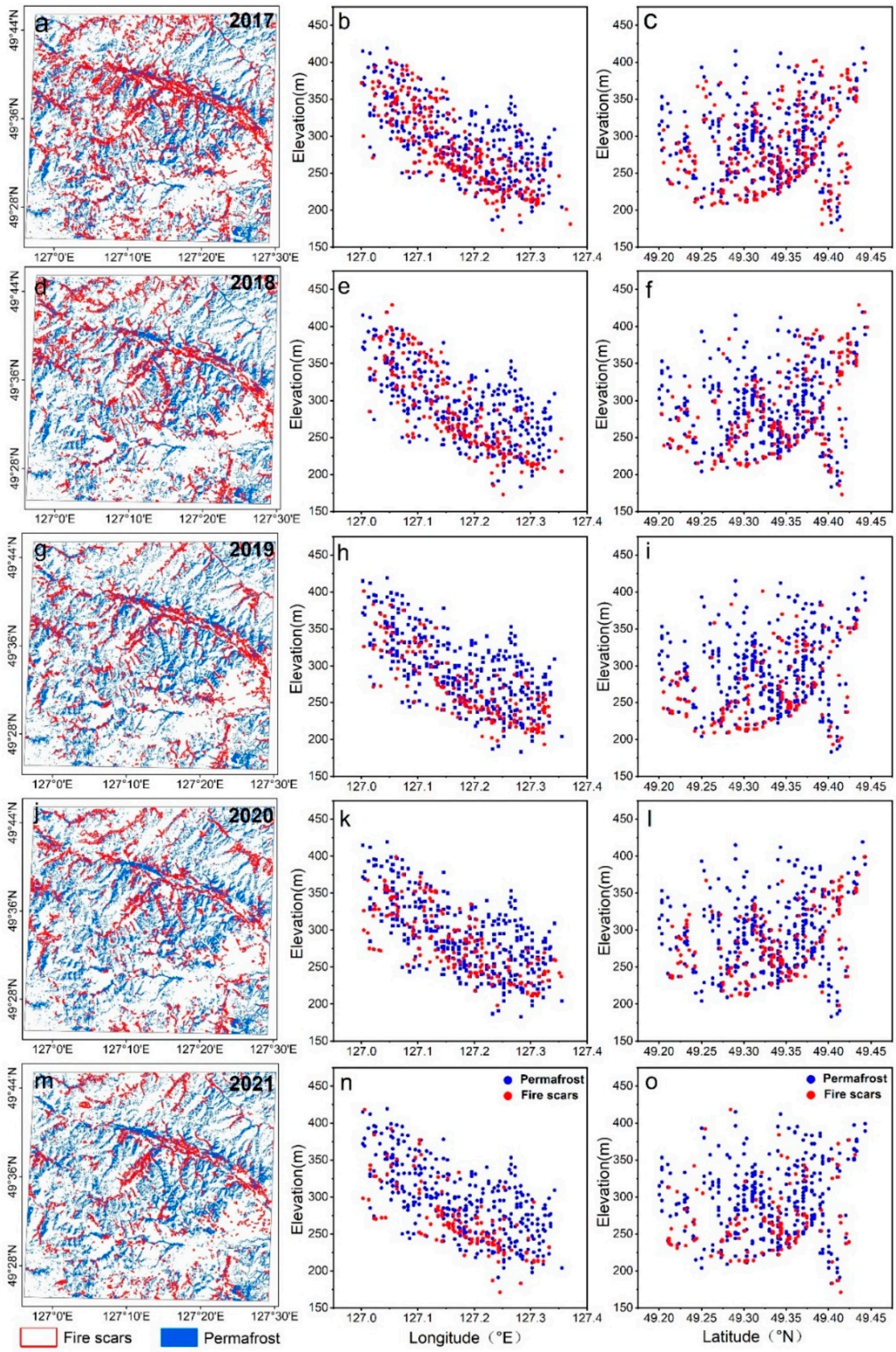

Figure 5. Spatial distribution of spring fire scars on permafrost from 2017 to 2021, and the elevation-longitude distribution, the elevation-latitude distribution. (**a**) Spatial distribution of fire scars on permafrost in 2017. (**b**) The elevation-longitude distributions of fire scars and permafrost in 2017. (**c**) The elevation-latitude distributions of fire scars and permafrost in 2017. (**d**–**f**) Spatial distribution in 2018. (**g**–**i**) Spatial distribution in 2019. (**j**–**l**) Spatial distribution in 2020. (**m**–**o**) Spatial distribution in 2021.

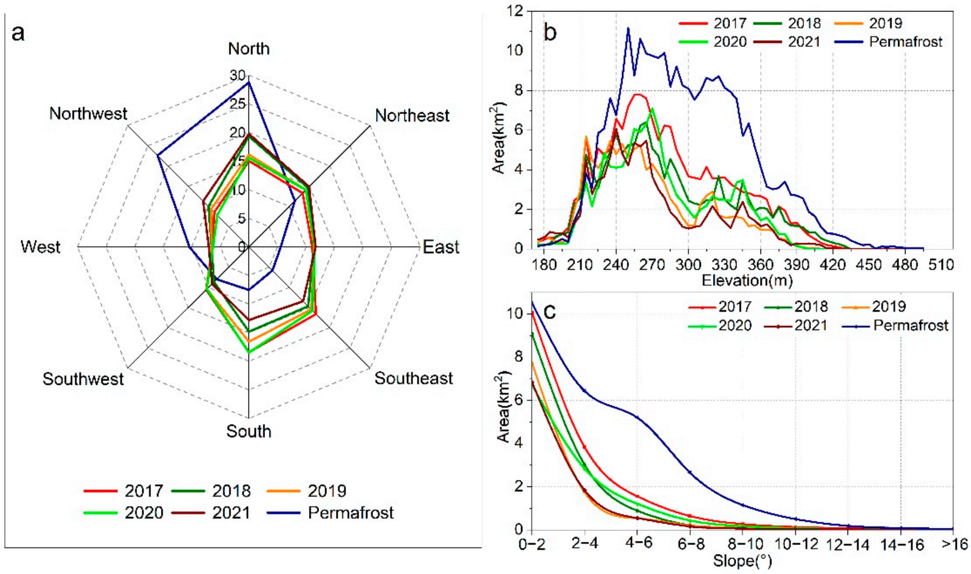

Figure 6. Distribution of spring fire scars and permafrost in terms of aspect, altitude, and slope. (**a**) The proportions of fire scars and permafrost on each aspect in 2017–2021. (**b**) The distribution of fire scars with altitude. (**c**) The distribution of fire scars with slope.

3.3. Seasonal Climate Change and Methane Emission Patterns

From 2017–2020, the average annual air temperature in the study area remained at approximately 1.8 °C (Figure 7b), with a steady increase at a rate of 6.3171×10^{-4} °C/a; the maximum and minimum values occurred in 2020 (2.3 °C) and 2018 (1.1 °C), respectively, and the temperature generally reached the maximum in July each year. The average annual air humidity was 51.163% (Figure 7a), with a rate of increase of 0.3912%/a. The air humidity in the year shows a fluctuating trend of first decreasing, then increasing and then decreasing. The air humidity in the study area significantly decreased in spring each year, reaching an annual minimum at the end of March and the beginning of April. In the following two months, the air humidity increased rapidly and reached its annual maximum in July. Humidity declined from August to October but remained higher than in the spring.

In permafrost regions, the large amount of meltwater generated at the beginning of snowmelt in spring causes the air humidity to rise rapidly in a short period of time. However, because the surface has not yet thawed and is blocked by the permafrost, the meltwater cannot fully replenish the soil moisture, and the gradually increasing temperature leads to abnormal loss and evaporation of meltwater not absorbed by the soil layer, resulting in a stronger response of soil moisture to temperature increase in permafrost regions than in nonpermafrost regions [23]. Therefore, there was a short period of decline in humidity in the study area in early April.

The methane concentration monitoring data from the R-1 meteorological station from 2017–2020 and the R-2 meteorological station from 2019–2020 (Figure 7d) show that the methane concentration changes within a year can be divided into three phases, namely, March–May, June–August, and September–November. The phase of short-term release of high concentrations of methane occurred in late March and early April of each year, during which methane concentration reached its highest level in the year (over 1000 ppm in 2017, 2018, and 2019). As the temperature rose in spring, the ground snow and ice cover gradually melted, and the relatively low pressure promoted the short-term release of a large amount of methane gas enclosed in the active layer of permafrost because of the frozen surface in winter. From June to August, due to the surface thaw and the effect of methanogens in swamps, methane gas was in the phase of sustained release at moderate concentrations, with methane concentrations at the R-1 meteorological station remaining at 200–400 ppm in 2017 and 2018. The period from September to November was the phase of short-term emission of high concentrations of methane in the study area. During this phase, the upper surface of the active layer gradually froze, the ground snow cover gradually increased, and the methane gas that had accumulated between the active layer and the upper limit of permafrost through production by methanogens was perhaps squeezed out by frost, resulting in a high concentration of methane on the surface in a short period of time [41].

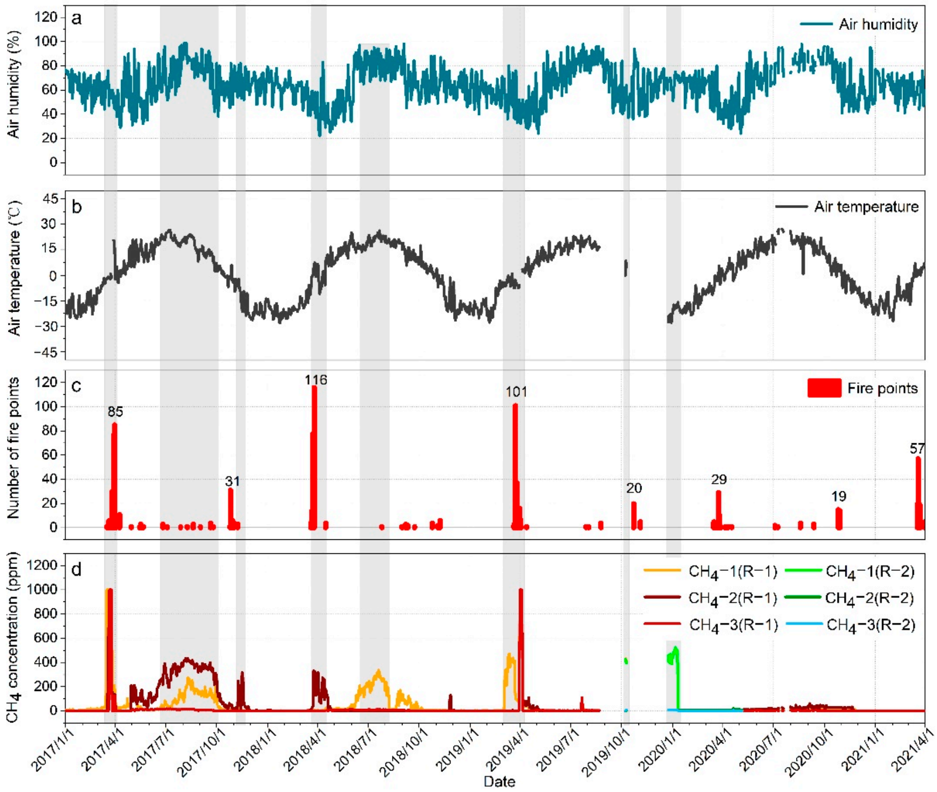

Figure 7. Curves of temporal variation in air humidity and surface air temperature at the R-1 meteorological station as well as surface methane concentrations at three monitoring points at each of the R-1 and R-2 meteorological stations in the study area. (**a**) The curve of average daily air humidity variation from January 2017 to April 2021. (**b**) The curve of average daily surface air temperature variation. (**c**) The number of daily fires in the study area. (**d**) The curves of variation in average daily methane concentrations at the R-1 and R-2 meteorological stations, with three methane concentration sensors installed at each station. The background shows the high-concentration methane emission phase (with a surface methane concentration of ≥200 ppm).

The release of highly concentrated methane was detected at the R-2 meteorological station in January 2020, probably because the incomplete freezing of the upper surface or the continued thawing of the frozen layer led to an early release of the methane accumulated in high concentration in the soil. After January 2020, the surface methane concentrations at the R-1 and R-2 meteorological stations gradually tended towards low values, which was related to the special surface cover conditions near the monitoring points (Figure 2). According to a previous study by Guo et al. on the degradation of permafrost in the study area between September 2009 and October 2016, under the influence of climate change and engineering construction disturbance, the permafrost in the study area is degrading, and the degradation method is that the permafrost table and permafrost base changes synchronously, and the rising speed of the permafrost base exceeds the decline rate of the permafrost table. The thickness of permafrost gradually declined, and permafrost may further degrade to disappear completely in the coming years [27,42]. The annual degradation of permafrost lowered the water table, which led to reduced soil moisture and a zone of elevated CH_4 oxidation, in turn resulting in decreasing methane emissions in some regions [43,44].

3.4. Analysis of the Relationships of Seasonal Climate Change and Methane Emissions with Wildfires

To investigate the relationship between methane concentration and wildfires, the number of daily fires in the study area from 2017 to 2020 was extracted using the VIIRS Active Fire product (Figure 7c). The pattern of changes in the number of fires was consistent with that for methane concentration throughout the year, the period with the larger number of fire points corresponds to the two short-term emission periods of high methane concentration from March to April and September to November. The number of daily fire points from late March 2017 to 2019 was between 70 and 120, and the number of fire points from March to April accounted for 57% (2020) to 92% (2018) of the total number of fire points in the year. In 2020, the number of fire spots in the study area declined significantly, which corresponded to a decrease in methane concentration. This consistency between changes in wildfires and changes in methane concentration demonstrates that methane emission is an important factor affecting wildfire occurrence in permafrost regions.

Analysis of correlations of the number of fires per month in the study area with the air temperature, air humidity, and methane concentrations monitored by the three methane sensors at the R-1 meteorological station was conducted (Figure 8). There is a positive correlation between the methane concentration and the number of fire points, and the correlation coefficient between the two reached the maximum value during the year in March and April—especially in March 2018 and April 2019, when the number of fire points and methane concentration showed a very significant positive correlation ($R^2 > 0.496$, $p < 0.01$).The air temperature is positively correlated with the number of fire points, and there is a very significant positive correlation between March 2017, March 2018, and April 2019. Spring air temperature and surface methane concentration in the study area have a strong impact on the occurrence of wildfires, and the frequency of wildfires increases with the increase of the two during this time period. There is a low negative correlation between air humidity and the number of fire points, but the two were significantly negatively correlated in March 2017 and March 2019 ($R^2 = 0.409$, $p < 0.05$; $R^2 = 0.375$, $p < 0.05$). Greater air humidity is not conducive to wildfires.

The highest frequency of wildfires occurred in late March and early April (Figure 9). During this period, the air humidity decreased significantly at rates of 0.591%/d (2017), 0.622%/d (2018), 0.490%/d (2019), and 0.752%/d (2020). The air humidity fluctuated greatly, increasing rapidly with the rapid increase in methane concentration and the occurrence of fires for a short period of time at the beginning of ice and snow melting, and then decreasing significantly. After that, the air humidity gradually increased but did not recover to the value before the wildfire in a short time, because the continuous high temperature after the fire accelerated the evaporation of soil moisture. In addition, due to the lack of precipitation and water supplement after the snow melting period, the humidity in this period was low. The air temperature increased in March and April at rates of 0.248 °C/d, 0.354 °C/d, 0.184 °C/d, and 0.349 °C/d, respectively, in 2017, 2018, 2019, and 2020. When there was no fire, the air temperature increased modestly; during the fire the temperature increased sharply.

The peaks of methane concentration at R-1 monitoring points occurred at 15–25 March (2017), 24–27 March (2018), and 30 March–6 April (2019), with average daily methane concentrations up to 1000 ppmv. The fires occurred after or along with the emission of high-concentration methane; during these times, the air temperature attained the highest values during the observation period, even reaching approximately 20 °C on 29 March 2017. The trend of variation in air humidity during this period was consistent with that for methane concentration, and the "greenhouse effect" produced by high methane concentration accelerated evaporation from the ground, causing a brief increase in air humidity. It is worth noting that the dates of large fires in 2018 coincided exactly with those of high methane concentrations, both occurring on 24–26 March. The year 2020 saw low methane concentrations at the monitoring points and a significant decrease in the number of fires over the entire region. Except for 2018, there was some difference between the dates of large fires and those of high methane concentrations. The main reason for this difference is that the fire statistics were calculated for the entire study area, while the surface methane concentrations were measured at monitoring points, and there could be some temporal differences between the timing of high-concentration methane releases at the R-1 and R-2 meteorological stations and that for the study area as whole.

The daily mean changes in air temperature, air humidity, and surface methane concentration indicated that the date of maximum surface methane concentration often preceded the fire, and the maximum air temperature slightly lagged behind the peak methane concentration, occurring at the time of the fire and after the fire. Air humidity rises briefly at the onset of the fire and then drops sharply to smaller values. This hot and dry environment provides favorable conditions for the spread of wildfires. In addition, the timing of wildfire occurrence in the spring of each year largely coincided with the periods of peak methane concentration, which further demonstrates that the rapid warming caused by high concentrations of methane emissions during permafrost thawing may increase the risk of wildfires in the spring, and that the flammability of methane itself is another condition that promoted the occurrence and spread of wildfires.

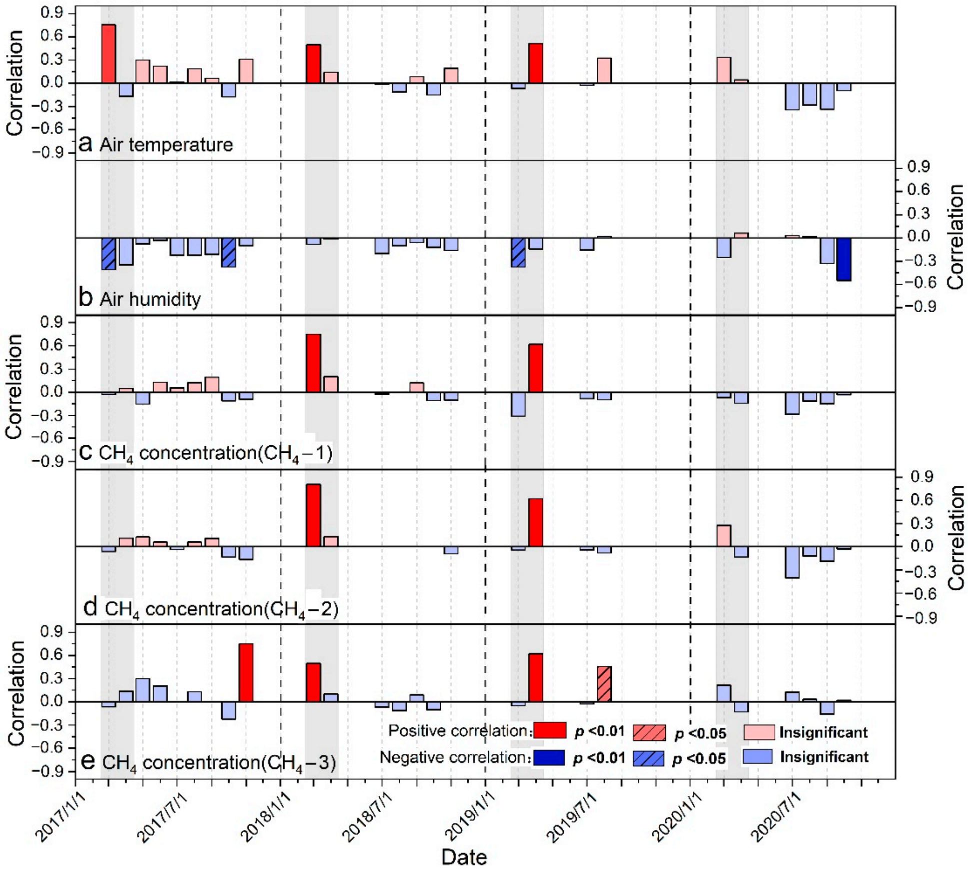

Figure 8. Correlation analysis of air temperature, air humidity, surface methane concentration, and the number of VIIRS fire points in the R-1 meteorological station. The red and blue colors indicate positive and negative correlations, respectively, between the influencing factors and number of fire points. The grey background shows the period of March to April of each year. (**a**) Correlation coefficient between air temperature and the number of VIIRS fire points. (**b**) Correlation coefficient between air humidity and the number of VIIRS fire points. (**c**–**e**) Correlation coefficient of methane concentration of CH_4-1, CH_4-2, and CH_4-3 with the number of VIIRS fire points.

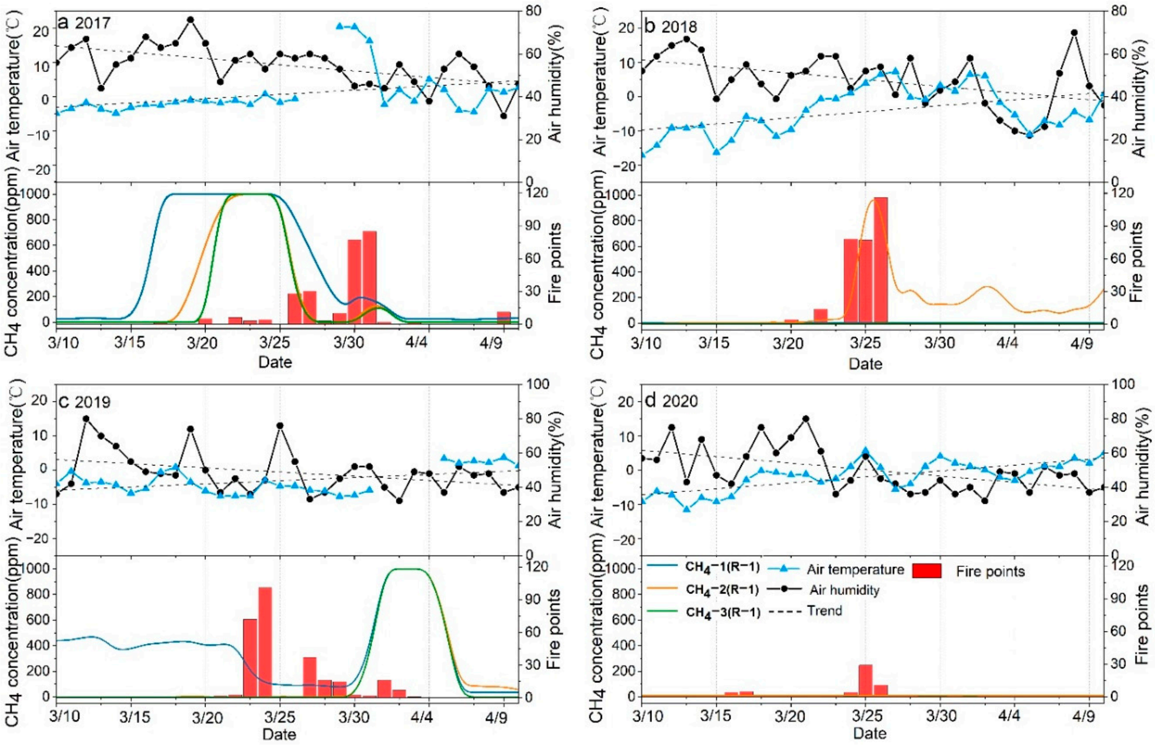

Figure 9. (**a**) In 2017, (**b**) 2018, (**c**) 2019, and (**d**) 2020, the change curve of air temperature, air humidity, and atmospheric methane concentration during the spring wildfire of the R-1 meteorological station, as well as the histogram of the number of daily fire points in the study area. The blue curve is the average daily air temperature, the black curve is the average daily air humidity, the red histogram shows the number of daily fires, and the curves of other colors are the methane concentration variation curves.

4. Discussion

4.1. Influence of Seasonal Permafrost Thaw on Methane Emissions

Affected by factors such as climate change and human activities, the thickness of permafrost in the northern Xiaoxing'an Mountains is gradually decreasing [42], and the organic matter and methane hydrates stored in permafrost are gradually entering the atmosphere in the form of methane gas [27]. The highest concentrations of surface methane emissions occurred in each spring (March to May), during which the methane gas from the decomposition of organic carbon in the active layer and methane hydrates from the destabilisation of permafrost are the main sources of high-concentration methane gas entering the atmosphere [45–47]. The seasonal frozen layer over the permafrost in winter hinders gas exchange between the soil and the atmosphere, causing the methane oxidation in winter to be only 5–15% of that in summer; the continued methane production from permafrost begins to accumulate under the frozen layer and snow cover, and large amounts of high-concentration, high-pressure methane gas are stored under the seasonal frozen layer or in the melting interlayer before being released [48,49].

During the short period of spring thaw, the methane stored in the frozen layer is released in stages. Since nutrients for methane-oxidizing bacteria may be at low levels during the thawing period, most of the accumulated methane escapes microbial oxidation and directly enters the atmosphere. In a study conducted by Michmerhuizen et al. [50], only 7% of methane was lost due to oxidation, and over 85% was directly released within 48 h after ice melting. Song et al. studied methane in the Sanjiang Plain in Northeast China and concluded that the spring thaw effect causes large methane emissions from permafrost regions [51]; in addition, the peak methane emissions in the spring thaw period can exceed the methane emissions in the growing season by three orders of magnitude, which is consistent with the methane concentrations observed in this study.

4.2. Local Methane Emissions and Wildfire Occurrence Patterns

In previous studies on fires in permafrost regions, high temperature and drought have been considered the main factors triggering fires [23], and the increase in forest fires in permafrost regions is attributed to temperature increases, which lead to earlier melting of snow cover in spring, increased evaporation, earlier ground exposure, and dry ground, thereby promoting the spread of fires [52] However, the spring wildfires in the northern Xiaoxing'an Mountains mainly occurred in swamp wetlands, which accounted for 16.81% of the total area of the study area. Seasonal changes in topsoil moisture in these regions are mainly driven by freeze–thaw cycles of seasonally frozen soil, with surface moisture usually having higher values during snow thaw in spring [53]. In this climate, the concentration of wildfires is also related to other conditions such as burning materials. We found that wildfires in the field were characterized by incomplete combustion of *Carex* (Figure 2); the *Carex* roots above the water surface in swamps burned to a high degree, while the *Carex* at the edges of waterbodies burned to a low degree, thereby resulting in the patchy distribution of fire scars centered on *Carex* (Figure 2g,h). In early spring, the frozen layer and snow cover had not completely melted, and the pore channels in the root system of *Carex* caused methane gas to be first emitted from these regions into the atmosphere. Due to the spatial heterogeneity in the growth and distribution of *Carex* and the difference in the distribution of permafrost, the concentration of methane entering the atmosphere was not uniformly distributed, thus leading to a difference in the degree of burning. In some areas, the methane gas concentration was low and, hence, *Carex* was not fully burned and appeared black. In some areas with many microvolcano-like features (Figure 2i), the *Carex* burned heavily and was grey in color, which was due to the extent of burning caused by the methane gas under the frozen layer breaking through the weak soil layer at high pressure resulting in high concentrations of methane gas discharged out of the pores.

Factors such as weather and climate are considered top-down drivers, while bottom-up drivers are local variables that influence fuel sources [54,55]. Methane gas has a greater warming potential when combined with aerosols (e.g., dust, sea salt, sulfate, black carbon, and other atmospheric particles). Therefore, methane gas may increase the risk of forest fires in degraded permafrost regions, due to its spontaneous combustion, and increase the regional atmospheric temperature [46]. Because of the large amount of carbon and heat emissions due to the occurrence of wildfires, the greenhouse warming due to promotion by methane of wildfires may be much higher than its direct contribution to the greenhouse effect. Previous research has found that, in addition to high temperature and drought, the high carbon emission flux from boreal peatlands plays a large feedback role in forest fires [14]. The pattern and mechanisms of wildfire occurrence in the area investigated in this study are similar to those in southeastern Siberia, reaching local peaks in spring and autumn, with the peaks in spring approximately 3–4 times those in autumn [23]. Large-scale wildfires also occur annually in spring in the southwest (Zeya-Bureya Basin) and southeast of the Bureya Mountains, Russia, which are adjacent to the Heilongjiang River in this study area. This region is a sedimentary basin with conditions for methane hydrate formation and storage; in addition, this region is adjacent to the area investigated in this study, located at the southern margin of the Eurasian permafrost zone, and is in a degraded permafrost zone with relatively unstable permafrost [27]. In addition to climatic factors, local methane emissions in permafrost regions are closely related to wildfires, and are synchronized in time and space, but the interaction mechanism between the two and the quantification of the correlation between the two need to be more comprehensive and require extensive data support and experimental validation.

4.3. Repeated Wildfire

Because wildfires cause rapid consumption of high-concentration methane, depletion of combustibles, and destruction of the microbial environment within the soil, it is generally believed that there will be no more wildfires in a region in the short term after a burn. However, the results of overlap analysis (Figure 10a) showed that repeated wildfires occurred in many areas during the monitoring period, and there were even sequences of more than three repeated fires. On the one hand, repeated wildfires occurred because wildfires destroyed the recovery mechanism of permafrost, and fires significantly impacted soil temperature and permafrost thaw depth. Studies have shown that several years after a fire event, the soil temperature of a burned plot remained higher than that of a control plot and the permafrost thaw depth was also deeper than that of the control plot; the active layer thickness of permafrost continued increasing for 25–50 years after the fire event [22,56]. On the other hand, with the continuous warming of the climate, the recovery ability of the permafrost temperature field is diminishing, and fires can have a compounding effect that accelerates the existing rate of permafrost degradation [57]. When the upper limit of permafrost drops to a critical depth, the overlying peat layer will not completely refreeze in the following winter, leading to further development of the active layer and formation of the thawing interlayer [15,58]. The slow recovery mechanism of permafrost cannot keep up with the effects of warming and fires. Therefore, methane gas continues to be produced in some regions in the winter after wildfires, triggering wildfires after the snow cover melts in the spring. For regions with intermittent wildfires and those where fires occur only once, methane is still emitted in spring but does not reach the concentration that would allow spontaneous combustion. The statistical analysis of the altitudinal distribution of repeated wildfires (Figure 10d) shows that repeated wildfires were mainly found at altitudes of 200–280 m. Within this altitude range, the percentages of the areas of ranges with sequences of 2, 3, 4, and 5 wildfires were 86.56%, 67.09%, 77.97%, and 22.53%, respectively, indicating that repeated fires were more likely to occur in low-altitude regions and that the permafrost in these regions was extremely unstable and degraded year after year. In addition, the superposition and correlation analysis showed that the number of wildfire occurrences was positively correlated with the area of permafrost (R^2 = 0.316). Multiple repeated wildfires occurred mainly in large areas of permafrost islands with high continuity at the landscape scale, consistent with a previous finding that regions with greater permafrost thickness and higher surface methane concentrations correspond to more severe burning [27]. For permafrost regions with discontinuous, sporadic, and patchy distributions, severe fires may cause years of damage and loss [59,60].

4.4. Uncertainty of the Investigation

First, due to the limitation of the spatial and temporal resolution of remote sensing data as well as the interference of weather, it is difficult to refine the inversion of permafrost distribution, and the inversion results are subject to human intervention. So far, only local areas of Xiaoxing'an Mountains have been selected for the study. This interaction between fire occurrence and permafrost degradation needs to be further verified across the entire boreal region. Second, there is a certain time lag between permafrost data and wildfire data. At the beginning of the study, we drew the permafrost distribution map of the study area in 2009 and 2017–2020 based on Landsat data, but according to the verification results of field drilling data and weather station data, the permafrost distribution data in 2009 is better than the other period's data. Although permafrost may have changed in some areas, this data basically reflects the spatial distribution of permafrost in our study area, and its more accurate spatio-temporal correlation with wildfires is indeed worthy of further study. In the next plan, we will improve the simulation method of permafrost distribution, obtain updated permafrost data, study the occurrence law of wildfires in the permafrost degradation zone, and analyze the internal relationship between the two.

In addition, because the monitoring environment is in areas of permafrost, the instruments at the meteorological stations are greatly affected by environmental factors such as low temperature as well as snow and ice; therefore, the accuracy of the instruments must be calibrated regularly and there are problems of missing data. It is necessary to increase the number of meteorological stations to form a monitoring network in order to achieve a comprehensive monitoring of methane gas emissions and their impact on wildfires in permafrost regions. However, our current preliminary experiments can still reveal some important information about fires, permafrost degradation, and methane emissions in permafrost regions, and their correlations.

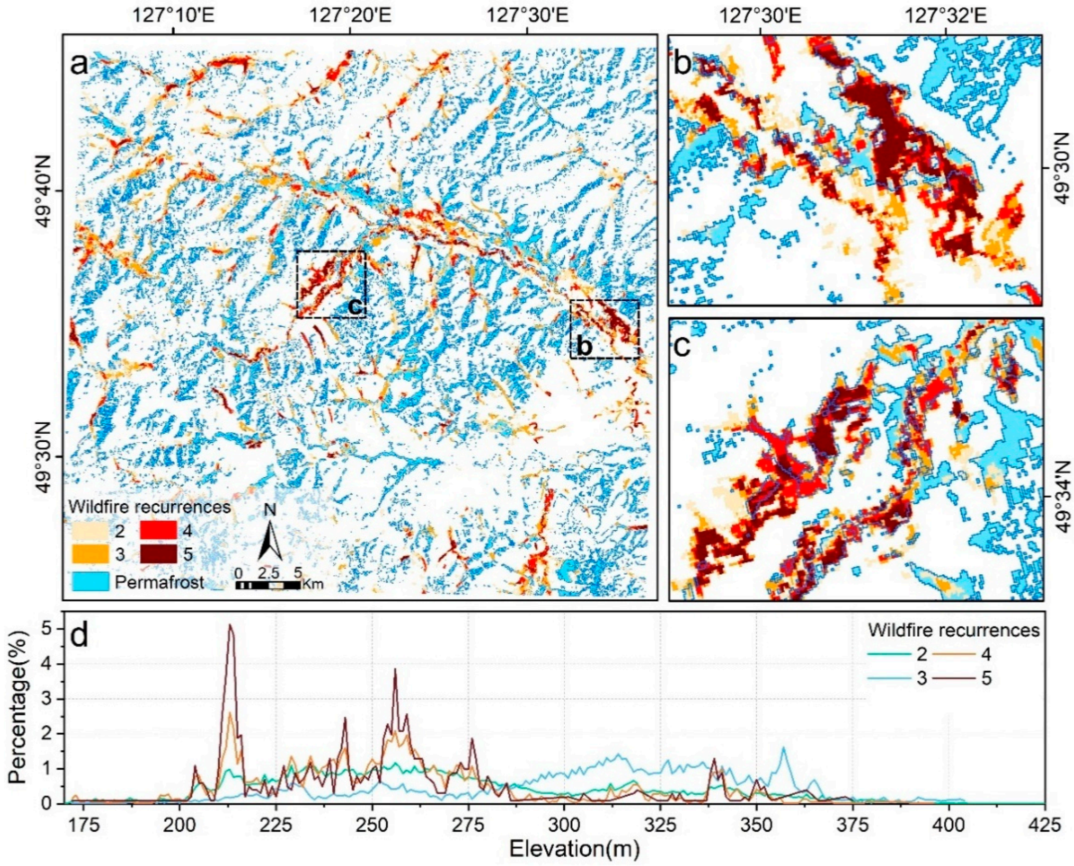

Figure 10. Spatial distribution of repeated wildfires in the study area from 2017 to 2021, obtained by superposition analysis of fire scars. (**a**) is the spatial distribution of repeated wildfires from 2017 to 2021 obtained from the overlay analysis, and the number of repeated wildfires is 2–5. (**b**,**c**) are typical areas with multiple wildfires. Wildfires mostly occur on large permafrost islands and their spatial distribution is basically the same as that of island permafrost. (**d**) is the altitude distribution of repetitive wildfires. Note: The altitudinal distribution of repetitive wildfires is counted pixel by pixel, which reflects the regionality of permafrost degradation. The degradation degree of permafrost at low altitudes (basins and lowland wetlands) is significantly higher than that in high-altitude areas (upper mountains, mostly thawed soils) or permafrost-stunted areas.

5. Conclusions

Wildfires in the study area mostly occurred in spring and autumn, and the number of fire points in spring accounted for more than 57% of the total number of fire points in the year. Spring fire scars and permafrost are highly consistent in spatial distribution, with the largest distribution in low-lying wetlands at an altitude of about 250 m, with a gradually increasing distribution from west to east and from high to low. From 2017 to 2021, the spatial change of the fire scars reflects the development law of wildfires shifting from the southern slope to the north slope and spreading from high altitude to low altitude, which is also in line with the degradation law of Xing'an Baikal permafrost.

The surface methane concentration has three stages during the year. The maximum methane concentration in spring (March–May) can reach 1000 ppmv, which is three times the methane concentration in the second (June–August) and third stage (September–November). The annual average temperature rises steadily at a rate of 6.3171×10^{-4} °C/a, and the air humidity in the year shows a fluctuating trend of first decreasing, then increasing and then decreasing. The frequency of wildfires and methane concentration changes during the year are consistent. The early snowmelt in spring is a high-incidence period of wildfires. During this period, the number of fire spots in the study area reached the annual maximum, and the air methane concentration also reached the annual maximum. With wildfires and high concentrations of methane, air temperatures reach large values for a short period of time. Before and after the fire, the air humidity changed significantly in stages.

The number of fire points is positively correlated with air temperature and surface methane concentration, and the correlation coefficient has the maximum value in the year from March to April. The number of fire points in spring was significantly negatively correlated with air humidity. In addition to climatic factors, local methane concentration is also one of the main driving factors for the occurrence of spring wildfires in permafrost regions. The spring thaw effect leads to the concentrated emission of high-concentration methane. Wildfires mostly occur during or shortly after the release of high concentrations of methane.

Repeated wildfires mostly occur on large and continuous permafrost islands (at the landscape scale), and the number of wildfires is positively correlated with the permafrost area. The distribution, thickness, and changes of the active layer of permafrost affect the frequency, extent, and scope of wildfires to a certain extent. Repetitive wildfires are more likely to occur in low-altitude permafrost regions that are unstable and continue to degrade. The methane emissions and wildfire occurrence patterns in the process of permafrost degradation require more comprehensive observations in the future, and the relationship and mechanism between the two deserve further exploration and in-depth research.

Author Contributions: Conceptualization, W.S.; data curation, L.Q., Z.X. and S.L.; formal analysis, Y.G.; funding acquisition, W.S.; methodology, L.Q. and C.Z.; software, Y.G. and S.L.; writing—original draft, L.Q. and C.Z.; writing—review & editing, W.S., L.Q. and Z.X. All authors have read and agreed to the published version of the manuscript.

Funding: We thank the National Natural Science Foundation of China (Grant No. 41641024) and Science and the Technology Project of Heilongjiang Communications Investment Group (Grant No. JT-100000-ZC-FW-2021-0182) for providing financial support and the Field scientific observation and research station of the Ministry of Education–Geological Environment System of Permafrost Area in Northeast China (MEORS-PGSNEC).

Institutional Review Board Statement: Not applicable.

Informed Consent Statement: Not applicable.

Data Availability Statement: All data generated or analyzed during this study are included in this published article.

Conflicts of Interest: The authors declare no conflict of interest.

References

1. Liu, X.; Guo, Y.; Hu, H.; Sun, C.; Zhao, X.; Wei, C. Dynamics and controls of CO_2 and CH_4 emissions in the wetland of a montane permafrost region, northeast China. *Atmos. Environ.* **2015**, *122*, 454–462. [CrossRef]
2. Cooper, M.D.; Estop-Aragonés, C.; Fisher, J.P.; Thierry, A.; Garnett, M.H.; Charman, D.J.; Hartley, I.P. Limited contribution of permafrost carbon to methane release from thawing peatlands. *Nat. Clim. Chang.* **2017**, *7*, 507–511. [CrossRef]
3. Knorre, A.A.; Kirdyanov, A.V.; Prokushkin, A.S.; Krusic, P.J.; Büntgen, U. Tree ring-based reconstruction of the long-term influence of wildfires on permafrost active layer dynamics in Central Siberia. *Sci. Total Environ.* **2019**, *652*, 314–319. [CrossRef] [PubMed]
4. Schuur, E.A.; McGuire, A.D.; Schädel, C.; Grosse, G.; Harden, J.W.; Hayes, D.J.; Vonk, J.E. Climate change and the permafrost carbon feedback. *Nature* **2015**, *520*, 171–179. [CrossRef]
5. Slater, A.G.; Lawrence, D.M. Diagnosing present and future permafrost from climate models. *J. Clim.* **2013**, *26*, 5608–5623. [CrossRef]
6. Dickens, G.R. Down the rabbit hole: Toward appropriate discussion of methane release from gas hydrate systems during the Paleocene-Eocene thermal maximum and other past hyperthermal events. *Clim. Past.* **2011**, *7*, 831–846. [CrossRef]
7. Hautala, S.L.; Solomon, E.A.; Johnson, H.P.; Harris, R.N.; Miller, U.K. Dissociation of Cascadia margin gas hydrates in response to contemporary ocean warming. *Geophys. Res. Lett.* **2014**, *41*, 8486–8494. [CrossRef]

8. Burke, S.A.; Wik, M.; Lang, A.; Contosta, A.R.; Palace, M.; Crill, P.M.; Varner, R.K. Long-term measurements of methane ebullition from thaw ponds. *J. Geophys. Res. Biogeol.* **2019**, *124*, 2208–2221. [CrossRef]
9. MacDougall, A.H.; Avis, C.A.; Weaver, A.J. Significant contribution to climate warming from the permafrost carbon feedback. *Nat. Geosci.* **2012**, *5*, 719–721. [CrossRef]
10. McGuire, A.D.; Koven, C.; Lawrence, D.M.; Clein, J.S.; Xia, J.; Beer, C.; Zhuang, Q. Variability in the sensitivity among model simulations of permafrost and carbon dynamics in the permafrost region between 1960 and 2009. *Glob. Biogeochem. Cycl.* **2016**, *30*, 1015–1037. [CrossRef]
11. Gibson, C.M.; Chasmer, L.E.; Thompson, D.K.; Quinton, W.L.; Flannigan, M.D.; Olefeldt, D. Wildfire as a major driver of recent permafrost thaw in boreal peatlands. *Nat. Commun.* **2018**, *9*, 3041. [CrossRef]
12. Flannigan, M.; Stocks, B.; Turetsky, M.; Wotton, M. Impacts of climate change on fire activity and fire management in the circumboreal forest. *GCB Bioenergy* **2009**, *15*, 549–560. [CrossRef]
13. Nitze, I.; Grosse, G.; Jones, B.M.; Romanovsky, V.E.; Boike, J. Remote sensing quantifies widespread abundance of permafrost region disturbances across the Arctic and Subarctic. *Nat. Commun.* **2018**, *9*, 5423. [CrossRef] [PubMed]
14. Köster, E.; Köster, K.; Berninger, F.; Prokushkin, A.; Aaltonen, H.; Zhou, X.; Pumpanen, J. Changes in fluxes of carbon dioxide and methane caused by fire in Siberian boreal forest with continuous permafrost. *J. Environ. Manag.* **2018**, *228*, 405–415. [CrossRef] [PubMed]
15. Ackley, C.; Tank, S.E.; Haynes, K.M.; Rezanezhad, F.; McCarter, C.; Quinton, W.L. Coupled hydrological and geochemical impacts of wildfire in peatland-dominated regions of discontinuous permafrost. *Sci. Total Environ.* **2021**, *782*, 146841. [CrossRef]
16. Sukhinin, A.I.; French, N.H.; Kasischke, E.S.; Hewson, J.H.; Soja, A.J.; Csiszar, I.A.; Slinkina, O.A. AVHRR-based mapping of fires in Russia: New products for fire management and carbon cycle studies. *Remote Sens. Environ.* **2004**, *93*, 546–564. [CrossRef]
17. Nelson, K.; Thompson, D.; Hopkinson, C.; Petrone, R.; Chasmer, L. Peatland-fire interactions: A review of wildland fire feedbacks and interactions in Canadian boreal peatlands. *Sci. Total Environ.* **2021**, *769*, 145212. [CrossRef]
18. Chen, Y.; Romps, D.M.; Seeley, J.T.; Veraverbeke, S.; Riley, W.J.; Mekonnen, Z.A.; Randerson, J.T. Future increases in Arctic lightning and fire risk for permafrost carbon. *Nat. Clim. Chang.* **2021**, *11*, 404–410. [CrossRef]
19. Dindaroglu, T.; Babur, E.; Yakupoglu, T.; Rodrigo-Comino, J.; Cerda, A. Evaluation of geomorphometric characteristics and soil properties after a wildfire using Sentinel-2 MSI imagery for future fire-safe forest. *Fire Saf. J.* **2021**, *122*, 103318. [CrossRef]
20. Silva, S.S.; Fearnside, P.M.; Alencastro Graça, P.M.L.; Brown, I.F.; Alencar, A.; Melo, A.W.F. Dynamics of forest fires in the southwestern Amazon. *For. Ecol. Manag.* **2018**, *424*, 312–322. [CrossRef]
21. Gao, H.; Nie, N.; Zhang, W.; Chen, H. Monitoring the spatial distribution and changes in permafrost with passive microwave remote sensing. *ISPRS J. Photogramm.* **2020**, *170*, 142–155. [CrossRef]
22. Heim, R.J.; Bucharova, A.; Brodt, L.; Kamp, J.; Rieker, D.; Soromotin, A.V.; Hölzel, N. Post-fire vegetation succession in the Siberian subarctic tundra over 45 years. *Sci. Total Environ.* **2021**, *760*, 143425. [CrossRef] [PubMed]
23. Kim, J.S.; Kug, J.S.; Jeong, S.J.; Park, H.; Schaepman-Strub, G. Extensive fires in southeastern Siberian permafrost linked to preceding Arctic Oscillation. *Sci. Adv.* **2020**, *6*, eaax3308. [CrossRef] [PubMed]
24. Zhang, Y.; Wu, Q.B.; Liu, J.P. Distribution characteristics of the permafrost in the section from Heihe to Bei'an in the Xiao Hinggan Mountains. *J. Glaciol.* **2001**, *23*, 312–317. (In Chinese with English abstract)
25. Jin, H.J.; Yu, S.P.; Guo, D.; Lv, L.Z.; Wu, L.Y.; Sun, G.; Yu, Q. Degradation of permafrost in the Da and Xiao Hinggan Mountains, Northeast China, and preliminary assessment of its trend. *J. Glaciol.* **2006**, *28*, 467–476. (In Chinese with English abstract)
26. Jin, H.J.; Wang, S.L.; Lv, L.Z.; Yu, S.P. Features of permafrost degradation in Hinggan Mountains, northeastern China. *Sci. Geol. Sin.* **2009**, *2*, 223–228. (In Chinese with English abstract)
27. Shan, W.; Xu, Z.; Guo, Y.; Zhang, C.; Hu, Z.; Wang, Y. Geological methane emissions and wildfire risk in the degraded permafrost area of the Xiao Xing'an Mountains, China. *Sci. Rep.* **2020**, *10*, 21297. [CrossRef]
28. Gruber, S. Derivation and analysis of a high-resolution estimate of global permafrost zonation. *Cryosphere* **2012**, *6*, 221–233. [CrossRef]
29. Yu, Q.H.; Bai, Y.; Jin, H.J.; Qian, J.; Pan, X. The study of the patchy permafrost along the Heihe-Bei'an highway in the Xiao Hinggan Mountains with ground penetrating radar. *J. Glaciol. Geocryol.* **2008**, *3*, 461–468. (In Chinese with English abstract)
30. Malenovský, Z.; Rott, H.; Cihlar, J.; Schaepman, M.E.; García-Santos, G.; Fernandes, R.; Berger, M. Sentinels for science: Potential of Sentinel-1, -2, and-3 missions for scientific observations of ocean, cryosphere, and land. *Remote Sens. Environ.* **2012**, *120*, 91–101. [CrossRef]
31. Gibson, R.; Danaher, T.; Hehir, W.; Collins, L. A remote sensing approach to mapping fire severity in south-eastern Australia using sentinel 2 and random forest. *Remote Sens. Environ.* **2020**, *240*, 111702. [CrossRef]
32. Wang, C.J.; Shan, M.N.; Hu, Z.G.; Shan, W. Multi-spectral remote sensing based land surface temperature retrieval and isolated permafrost zone segmentation. *Infrared Laser Eng.* **2015**, *44*, 1390–1396. (In Chinese with English abstract)
33. Chen, D.; Fu, C.; Hall, J.V.; Hoy, E.E.; Loboda, T.V. Spatio-temporal patterns of optimal Landsat data for burn severity index calculations: Implications for high northern latitudes wildfire research. *Remote Sens. Environ.* **2021**, *258*, 112393. [CrossRef]
34. Elvidge, C.D.; Zhizhin, M.; Hsu, F.C.; Baugh, K.; Khomarudin, M.R.; Vetrita, Y.; Hilman, D. Long-wave infrared identification of smoldering peat fires in Indonesia with nighttime Landsat data. *Environ. Res. Lett.* **2015**, *10*, 065002. [CrossRef]

35. Li, C.; Wu, P.T.; Li, X.L.; Zhou, T.W.; Sun, S.K.; Wang, Y.B.; Yu, X. Spatial and temporal evolution of climatic factors and its impacts on potential evapotranspiration in Loess Plateau of Northern Shaanxi, China. *Sci. Total Environ.* **2017**, *589*, 165–172. [CrossRef] [PubMed]
36. Asrari, E.; Masoudi, M.; Hakimi, S.S. GIS overlay analysis for hazard assessment of drought in Iran using Standardized Precipitation Index (SPI). *J. Ecol. Environ.* **2012**, *35*, 323–329. [CrossRef]
37. Shan, W.; Zhang, C.; Guo, Y.; Shan, M.; Zeng, X.; Wang, C. Climate Change and Surface Deformation Characteristics in Degradation Area of Permafrost in Lesser Khingan Mountain, China. In Proceedings of the Workshop on World Landslide Forum, Kyoto, Japan, 3 November 2020; Springer: Cham, Switzerland, 2020; pp. 209–219.
38. Song, X.; Wang, G.; Ran, F.; Chang, R.; Song, C.; Xiao, Y. Effects of topography and fire on soil CO_2 and CH_4 flux in boreal forest underlain by permafrost in northeast China. *Ecol. Eng.* **2017**, *106*, 35–43. [CrossRef]
39. Fang, L.; Yang, J.; White, M.; Liu, Z. Predicting potential fire severity using vegetation, topography and surface moisture availability in a Eurasian boreal forest landscape. *Forests* **2018**, *9*, 130. [CrossRef]
40. Zhang, Z.Q.; Wu, Q.B.; Hou, M.T.; Tai, B.W.; An, Y.K. Permafrost change in Northeast China in the 1950s–2010s. *Adv. Clim. Chang. Res.* **2021**, *12*, 18–28. [CrossRef]
41. Mastepanov, M.; Sigsgaard, C.; Dlugokencky, E.J.; Houweling, S.; Ström, L.; Tamstorf, M.P.; Christensen, T.R. Large tundra methane burst during onset of freezing. *Nature* **2008**, *456*, 628–630. [CrossRef]
42. Guo, Y.; Shan, W.; Zhang, C.; Hu, Z.; Wang, S.; Gao, J. Monitoring of permafrost degradation along the Bei'an-Heihe Expressway in China. *B Eng. Geol. Environ.* **2021**, *80*, 1–10. [CrossRef]
43. Song, X.; Wang, G.; Hu, Z.; Ran, F.; Chen, X. Boreal forest soil CO_2 and CH_4 fluxes following fire and their responses to experimental warming and drying. *Sci. Total Environ.* **2018**, *644*, 862–872. [CrossRef] [PubMed]
44. Lawrence, D.M.; Koven, C.D.; Swenson, S.C.; Riley, W.J.; Slater, A.G. Permafrost thaw and resulting soil moisture changes regulate projected high-latitude CO2 and CH4 emissions. *Environ. Res. Lett.* **2015**, *10*, 094011. [CrossRef]
45. Walter Anthony, K.M.; Anthony, P.; Grosse, G.; Chanton, J. Geologic methane seeps along boundaries of Arctic permafrost thaw and melting glaciers. *Nat. Geosci.* **2012**, *5*, 419–426. [CrossRef]
46. Knoblauch, C.; Beer, C.; Liebner, S.; Grigoriev, M.N.; Pfeiffer, E.M. Methane production as key to the greenhouse gas budget of thawing permafrost. *Nat. Clim. Chang.* **2018**, *8*, 309–312. [CrossRef]
47. Keuper, F.; Wild, B.; Kummu, M.; Beer, C.; Blume-Werry, G.; Fontaine, S.; Dorrepaal, E. Carbon loss from northern circumpolar permafrost soils amplified by rhizosphere priming. *Nat. Geosci.* **2020**, *13*, 560–565. [CrossRef]
48. Tokida, T.; Mizoguchi, M.; Miyazaki, T.; Kagemoto, A.; Nagata, O.; Hatano, R. Episodic release of methane bubbles from peatland during spring thaw. *Chemosphere* **2007**, *70*, 165–171. [CrossRef]
49. Phelps, A.R.; Peterson, K.M.; Jeffries, M.O. Methane efflux from high-latitude lakes during spring ice melt. *J. Geophys. Res. Atmos.* **1998**, *103*, 29029–29036. [CrossRef]
50. Michmerhuizen, C.M.; Striegl, R.G.; McDonald, M.E. Potential methane emission from north-temperate lakes following ice melt. *Limnol. Oceanogr.* **1996**, *41*, 985–991. [CrossRef]
51. Song, C.; Xu, X.; Sun, X.; Tian, H.; Sun, L.; Miao, Y.; Guo, Y. Large methane emission upon spring thaw from natural wetlands in the northern permafrost region. *Environ. Res. Lett.* **2012**, *7*, 034009. [CrossRef]
52. Ponomarev, E.I.; Kharuk, V.I.; Ranson, K.J. Wildfires dynamics in Siberian larch forests. *Forests* **2016**, *7*, 125. [CrossRef]
53. Brown, D.R.; Jorgenson, M.T.; Kielland, K.; Verbyla, D.L.; Prakash, A.; Koch, J.C. Landscape effects of wildfire on permafrost distribution in interior Alaska derived from remote sensing. *Remote Sens.* **2016**, *8*, 654. [CrossRef]
54. Walker, X.J.; Rogers, B.M.; Veraverbeke, S.; Johnstone, J.F.; Baltzer, J.L.; Barrett, K.; Mack, M.C. Fuel availability not fire weather controls boreal wildfire severity and carbon emissions. *Nat. Clim. Chang.* **2020**, *10*, 1130–1136. [CrossRef]
55. Natole, M., Jr.; Ying, Y.; Buyantuev, A.; Stessin, M.; Buyantuev, V.; Lapenis, A. Patterns of mega-forest fires in east Siberia will become less predictable with climate warming. *Environ. Adv.* **2021**, *4*, 100041. [CrossRef]
56. Soja, A.J.; Cofer, W.R.; Shugart, H.H.; Sukhinin, A.I.; Stackhouse Jr, P.W.; McRae, D.J.; Conard, S.G. Estimating fire emissions and disparities in boreal Siberia (1998–2002). *J. Geophys. Res. Atmos.* **2004**, *109*, D14. [CrossRef]
57. Zhang, Y.; Wolfe, S.A.; Morse, P.D.; Olthof, I.; Fraser, R.H. Spatiotemporal impacts of wildfire and climate warming on permafrost across a subarctic region, Canada. *J. Geophys. Res. Earth.* **2015**, *120*, 2338–2356. [CrossRef]
58. Shi, L.; Dech, J.P.; Liu, H.; Zhao, P.; Bayin, D.; Zhou, M. Post-fire vegetation recovery at forest sites is affected by permafrost degradation in the Da Xing'an Mountains of northern China. *J. Veg. Sci.* **2019**, *30*, 940–949. [CrossRef]
59. Li, X.Y.; Jin, H.J.; Wang, H.W.; Marchenko, S.S.; Shan, W.; Luo, D.L.; Jia, N. Influences of forest fires on the permafrost environment: A review. *Adv. Clim. Chang. Res.* **2021**, *12*, 48–65. [CrossRef]
60. Shur, Y.L.; Jorgenson, M.T. Patterns of permafrost formation and degradation in relation to climate and ecosystems. *Permafr. Periglac.* **2007**, *18*, 7–19. [CrossRef]